Spatially resolved GHz magnetization dynamics of a magnetite nano-particle chain inside a magnetotactic bacterium

Thomas Feggeler,[1] Ralf Meckenstock,[1] Detlef Spoddig,[1] Benjamin W. Zingsem,[1,2] Hendrik Ohldag,[3,4] Heiko Wende,[1] Michael Farle,[1,5] Michael Winklhofer,[6] and Katharina J. Ollefs[1]

[1] *Faculty of Physics and Center for Nanointegration Duisburg-Essen (CENIDE), University of Duisburg-Essen, 47048 Duisburg, Germany**

[2] *Ernst Ruska Centre for Microscopy and Spectroscopy with Electrons and Peter Grünberg Institute, Forschungszentrum Jülich GmbH, 52425 Jülich, Germany*

[3] *SLAC National Accelerator Laboratory, 94025 Menlo Park, CA, United States*

[4] *Department of Physics, University of California Santa Cruz, Santa Cruz CA 95064, United States†*

[5] *Kirensky Institute of Physics, Federal Research Center KSC SB RAS, Russia*

[6] *School of Mathematics and Science, University of Oldenburg, 26129 Oldenburg, Germany*

Understanding magnonic properties of non-periodic magnetic nanostructures requires real-space imaging of ferromagnetic resonance modes with spatial resolution well below the optical diffraction limit and sampling rates in the 5-100 GHz range. Here, we demonstrate element-specific Scanning Transmission X-ray Microscopy detected Ferromagnetic Resonance (STXM-FMR) applied to a chain of dipolarly coupled Fe_3O_4 nano-particles (40-50 nm particle size) inside a single cell of a magnetotactic bacterium, *Magnetospirillum magnetotacticum*. The ferromagnetic resonance mode of the nanoparticle chain driven at 6.748 GHz and probed with 50 nm X-ray focus size was found to have a uniform phase response but non-uniform amplitude response along the chain segments due to the superposition of dipolar coupled modes of chain segments and individual particles, in agreement with micromagnetic simulations.

I. INTRODUCTION

Magnonics deals with the controlled excitation and detection of spin waves in magnetic media [1–7]. Due to the low energy nature of spin wave quanta (magnons), magnonic devices have been suggested to overcome key challenges of current charge-based computer information processing, such as power consumption and heat dissipation [8]. Recently, magnetic nanoparticle chains were proposed as magnonic logic gates on the sub-micron scale, which would enable unprecedented transistor counts in a single central processing unit [9]. For visual control of the functionality of submicron-sized magnon-based logic devices, it is essential to have a technique that can probe the magnetization dynamics on the 1-100 GHz scale with few nm resolution to determine the local phase and amplitude of excited magnons. Real-time observations using scanning electron microscopy with polarization analysis [10] have reached a temporal resolution (1 ns) sufficient to track relatively slow (10^2 MHz) dynamic magnetization processes involving vortex cores in soft magnetic materials. Faster dynamical processes can be studied with pump-probe schemes repeated for a sequence of delay times with each repetition starting from the same initial state and accumulating many pump-probe pulse cycles in a stroboscopic procedure. Pump-probe schemes are used in time-resolved photoemission electron microscopy (PEEM) [11, 12] and ultrafast transmission electron microscopes [13, 14], capable of probing transient demagnetization dynamics of nanodiscs with sub-100 nm resolution and sub-picoseconds delay time resolution [15]. Here we use Scanning Transmission X-ray Microscopy detected Ferromagnetic Resonance (STXM-FMR), where the magnetic specimen is driven by a continuous wave excitation, while temporal sampling is performed stroboscopically at a higher harmonic [16, 17]. The technique offers element specificity, $\leq$ 50 nm spatial resolution, and sampling rates of tens of GHz, allowing for spatial detection of resonant responses at up to 10 GHz [16]. By exploiting these features of STXM-FMR, we were able to detect a spatially non-uniform ferromagnetic resonance mode across a single chain of magnetite (Fe_3O_4) nanoparticles in a magnetotactic bacterium. Thus, we demonstrate the feasibility to detect ferromagnetic resonance in a nanomagnetic system with $\leq$ 50 nm spatial resolution.

II. EXPERIMENTAL DETAILS

With the STXM-FMR setup at the Stanford Synchrotron Radiation Lightsource (SSRL), FMR excitations in the linear regime are measured element specifically by employing the X-ray Magnetic Circular Dichroism (XMCD) effect [19, 20] in the transverse XMCD geometry [18]. The XMCD effect, defined as difference in X-ray absorption of left and right hand circularly polarized X-rays, is a measure of the magnetization M of the probed material projected onto the k-vector of the inci-

* Present address: Advanced Light Source, Lawrence Berkeley National Laboratory, Berkeley CA 94720, United States; tfeggeler@lbl.gov

† Present address: Advanced Light Source, Lawrence Berkeley National Laboratory, Berkeley CA 94720, United States and Department of Material Sciences and Engineering, Stanford University, Stanford CA 94305, United States

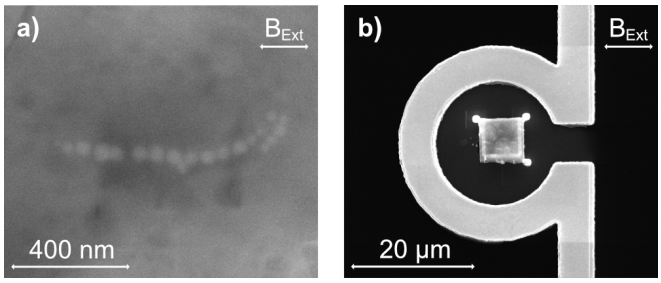

FIG. 1. a) Electron micrograph of the Fe_3O_4 nano-particle chain selected for STXM-FMR. The structure was deposited on a TEM grid and cut out with FIB. b) Cutout area including the nano-particle chain positioned in the center of the micro-resonator (light grey "omega" shape Au conduit). The direction of the magnetic field B_{Ext} is indicated.

dent X-rays. The resonant magnetic excitation is realized by applying linearly polarized continuous microwaves b_{mw} to the sample, polarized parallel to the propagation direction of the X-rays, while the static magnetic field B_{Ext} is orientated perpendicular to the k-vector of the X-rays. For the homogeneous excitation with high conventional detection sensitivity a micro-resonator setup is used [21].

The sample contains a chain of 19 Fe_3O_4 [23–26] nanoparticles with particle sizes of 40 - 50 nm [26] arranged in a segment of 15 particles and a smaller segment of 4 particles offset from this segment by a distance of about 25 nm (Figure 1 a). The nanoparticle chain grew naturally by biomineralization inside a bacterial cell of *Magnetospirillum magnetotacticum* [26–28]. The bacteria were obtained from Leibniz Institute DSMZ-German Collection of Microorganisms and Cell Cultures [22] as actively growing culture and positioned on a Transmission Electron Microscopy (TEM) grid (Figure 1 a). The grid with the nanoparticles was cutout by Focused Ion Beam (FIB) milling and placed at the center of the microresonator loop (Figure 1 b). The external magnetic field $B_{Ext} = 0.167 \pm 0.002$ T (Figure 1) corresponding to the resonance field predicted by our micromagnetic simulations, was applied in the sample plane along the direction of the chain axis as indicated in Figure 1. The sample was probed under dry conditions at room temperature at the Fe L_3-edge (708 eV [29]) with a focus of $\leq$ 50 nm, a step size of 25 nm and and a dwell time of five seconds per pixel with constant polarization of the X-rays. The microwave excitation at 6.748 GHz with a power of 25 dBm was chosen as the $(14+1/6)^{th}$ harmonics of the synchrotron frequency.

In the STXM-FMR measurements two sets of 6 consecutive images each are recorded pixel-by-pixel, which correspond to 6 images recorded with microwaves on and 6 images with microwave off, respectively. Between two consecutive images there is a time difference of 24.7 ps and a phase difference of ($\Delta\varphi = 60°$), yielding to the monitoring of 6 time steps of the microwave cycle [16]. To extract the microwave induced X-ray transmission the natural logarithm of the microwave off data divided by the microwave on data was taken. The data was normalized to the average intensity with consecutive minimum-maximum normalization. The phase and amplitude response at each pixel was obtained by fitting a sine function to the time dependent data [37]. The result is coded in the Hue-Saturation-Brightness (HSB) format to represent the phase relative to the time $t = 0$ ps as hue [30], the amplitude as brightness and the fit accuracy as saturation [37].

From the scanning electron micrographs (Figure 1 a), we designed a three-dimensional computer model of the nano-particle chain (single particle size 50 nm) using the micromagnetic simulation package MuMax3 [31, 32]. Taking into account the not perfectly stoichiometric Fe_3O_4 with the known decrease of the Verwey transition temperature [33], the saturation magnetisation M_{Sat} and the magnetocrystalline anisotropy constant K_1 [34], the dynamic simulation was calculated according to [34] with $M_{sat} = 465$ kA/m, and a first order cubic anisotropy constant $K_1 = -1.0 \times 10^4$ J/m^3. The exchange stiffness was set to $A = 1.32 \times 10^{-11}$ J/m [35] and the simulation grid was defined as 200 x 80 x 12 cells with a cell size of (5 nm)^3.

III. RESULTS AND DISCUSSION

In the FMR absorption spectrum simulated at 6.748 GHz (Figure 2 a), we observe three resonances at 0.169 T, 0.176 T and 0.187 T, which is surprising given that a linear chain usually behaves as a uniaxial magnet with one resonance mode per field orientation [36]. Evidently variations in the orientation and strength of the dipolar coupling between the particles in a chain produces complex magnon dispersion relations with multiple resonance lines and even magnonic band gaps, where resonances involving the same group of particles have incommensurate spatial mode profiles [9]. The variations in dipolar coupling are most pronounced in chain geometries with irregular particle spacings [9]. Indeed, for the chain at hand, the micromagnetic simulation confirms pronounced variations in dipolar coupling strength (Figure 2 b) along the chain axis, ranging from 0.450 T between adjacent particles (orange/red color) down to 0.050 T in the gap between the two chain segments. This essentially dynamically decouples the small four-particle segment on the left from the main chain segment. The decoupling becomes apparent in the snapshots of the dynamic micromagnetic simulation (Figure 2 c), where the oscillation amplitude is large in the main segment and small in the four-particle segment. Likewise, at the far right end of this chain, the oscillation amplitudes are comparatively small (Figure 2 c), which is due to the disturbance of the simple linear chain structure by two pairs of particles in side-by-side position perpendicular to the chain axis. In both side-by-side pairs, it is the lower particle that is more strongly coupled to the curved chain

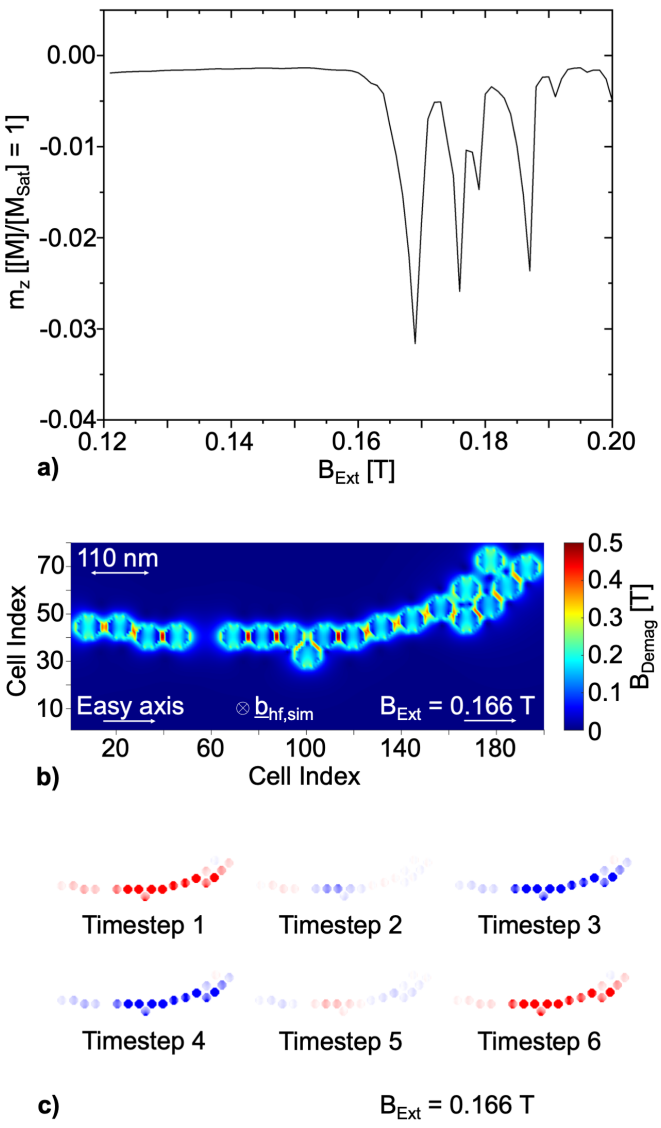

FIG. 2. a) Simulated FMR absorption spectrum in terms of the normalized m_z component of the magnetization over the field range B_{Ext} = 0.12 T - 0.2 T. b) Spatial distribution of the simulated inner demagnetization and outer stray-field at an applied static magnetic bias field of 0.166 T. c) Six timesteps ($\Delta t \sim 24.7$ ps) of the dynamic micromagnetic simulation, displaying a spatially inhomogeneous oscillation response. The normalized m_z-out-of-plane-component of the magnetization is color-coded (-z: blue, +z: red).

axis (compare with Figure 2 b), so that it can be excited more easily in the main resonance mode of the chain. Thus, on the basis of our micromagnetic simulations, we expect a non-homogeneous microwave response along the particle chain.

Indeed, the experimentally determined resonance amplitudes (Figure 3 a, c) are strongest (high brightness purple, white) in the main segment of the chain, but almost vanish in the left four-particle segment extending from x = 14 to x = 22 px at y = 10 px). Although individual particles cannot be resolved due to the limited focus (50 nm) at the Fe L_3, the upcurving bright white intensity pattern (x = 25 to x = 48 px and y = 6 to y = 12 px) tracks the curvature of the main segment of the chain. We note that in Figure 3a) and c) we find a non-zero phase and amplitude not only at the location of the chain but almost everywhere in the field of view. The reason for this observation is that there is a small crosstalk between the applied microwave and the (shielded) avalanche photodiode. Since the setup described in [16] represents a high quality factor lock-in amplifier tuned to the exciting microwave frequency, even the smallest fraction of microwave power at the diode will be detected. In consequence also without a sample a non-zero signal is observed. To remove the visibility of this background we discriminate the detected channel with a value of 250000 counts (see supporting information), revealing a clearly distinguishable resonant response of the particle chain with the highest amplitude along the upcurving chain segment. The phase map (Figure 3 a, b) reveals a largely uniform resonant response of the particle chain (270° to 300°) and is consistent with the time snapshots of the micromagnetic simulation (Figure 2 c). For comparison between experiment and theory, we evaluated the snapshot sequences from the micromagnetic simulations in the way as the experimental image sequences to obtain phase and amplitude maps (Figure 3 e and 3 f). All simulation results are pictured at B_{Ext} 166 mT, at which the best match to the experimental data is observed. Deviations between calculated and observed maps can be ascribed to the fact that not all small features of the 3D particles are reflected in the computer model, resulting in equally sized particles in the micromagnetic model, while the particle sizes and spacing in the real chain have some variability, particularly at the right end of the chain. This leads to variations in dipolar coupling strength (comp. Figure 2 b) and in consequence in the observed resonance modes.

The calculated phase response tallies with the observed one, except for the particle at the far upper right, which oscillates antiphasic to the rest of the chain (Figure 3 e), albeit with very low amplitude (Figure 3 f). As can be seen in the amplitude map, the response of the left four-particle segment indeed is weak, which explains the lack of signal in this region in the measured amplitude map. As inferred from the stray field map above (Figure 2 b), the particles that are vertically offset from the central chain axis and more weakly coupled to the chain, are weakly excited and thus have low oscillation amplitudes (Figure 3 f).

In summary, we observe a uniform phase but non-uniform amplitude response of the nano-particle chain. With the STXM-FMR technique, we thus demonstrate for the first time a measurement of a ferromagnetic resonance mode of a nano-particle chain in a spatially resolved manner ($\leq$ 50 nm). This technique allows to element-specifically examine the functionality of both periodic and non-periodic magnetic nanostructures of fu-

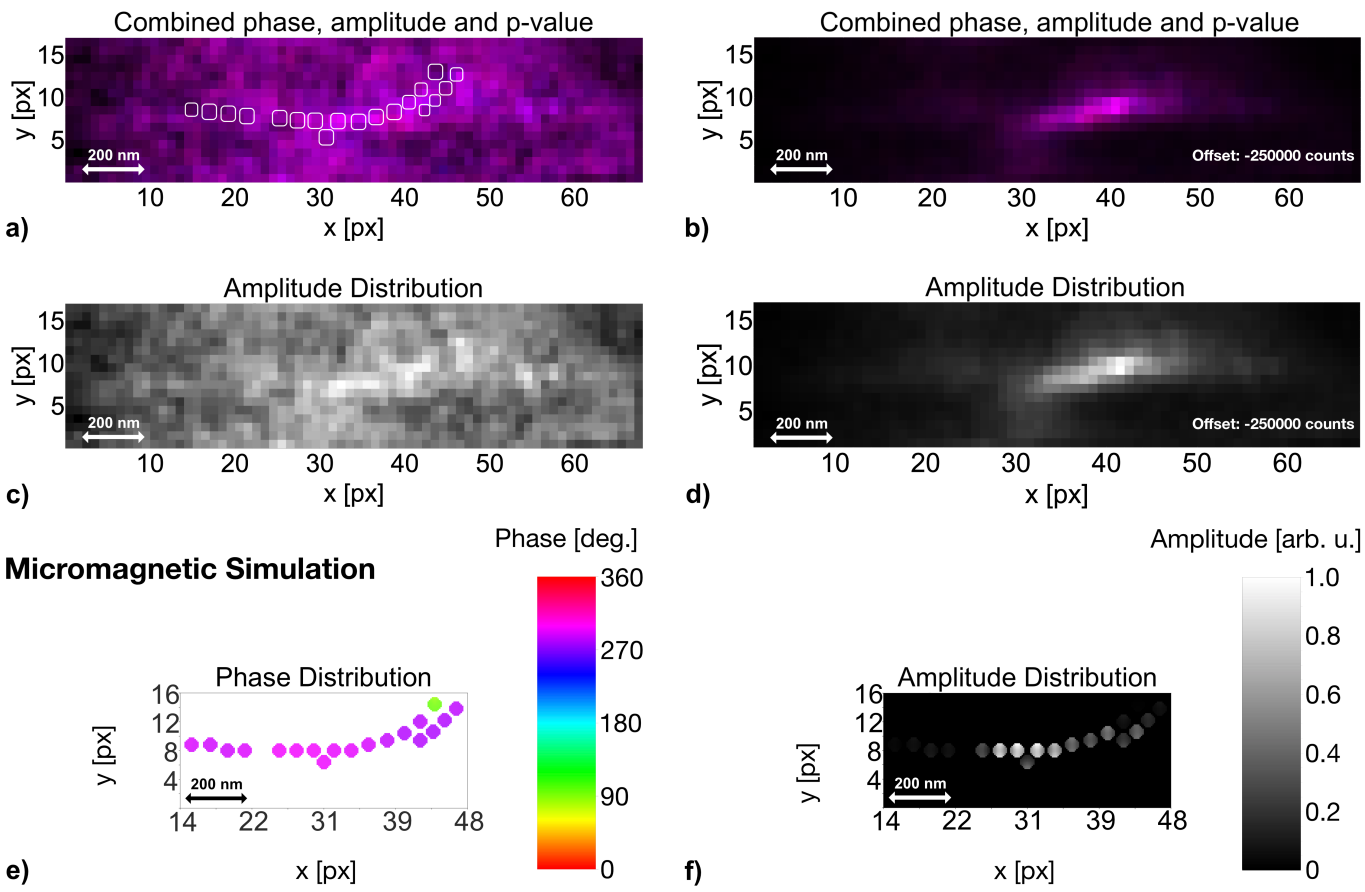

FIG. 3. a) Result of the pixel-by-pixel sinusoidal fit analysis for the STXM-FMR data at B_{Ext} 167 mT at f = 6.748 GHz. The phase relative to t = 0 ps, the amplitude and the fit accuracy are coded as hue, brightness and saturation. The estimated particle positions are indicated by rounded squares. b) Subfigure a) after subtraction of an offset of 250000 counts. c), d) Normalised amplitude distribution extracted from a), b) respectively. e), f) Phase and amplitude distribution of the micromagnetic simulation at B_{Ext} 166 mT at $f = 6.748$ GHz.

ture magnonic and spintronic devices, like for magnon spin transistors [39] and biomagnonics [9, 40], complementing spatially-resolved, non-element-specific, experimental techniques and micromagnetic simulations. A new STXM-FMR setup taking advantage of the increased spatial resolution of 10 nm [41] at the Advanced Light Source (ALS) will open the pathway to image X-band GHz magnetization dynamics of nanostructures on the $\leq$ 20 nm scale.

IV. ACKNOWLEDGEMENT

The authors thank the German Research Foundation (DFG project: OL513/1-1, 321560838) and the Austrian Science Fund (FWF project: I 3050-N36) for financial support. We gratefully acknowledge A. Ney for fruitful discussions. The use of the Stanford Synchrotron Radiation Lightsource, SLAC National Accelerator Laboratory, is supported by the U.S. Department of Energy, Office of Science, Office of Basic Energy Sciences under Contract No. DE-AC02-76SF00515.

V. SUPPORTING INFORMATION AVAILABLE:

Experimental information on the time resolved setup and considerations on the oscillating background.

[1] Chumak, A. V.; Serga, A. A. and Hillebrands, B., Magnonic crystals for data processing. *J. Phys. D: Appl. Phys.* **2017**, 50, 244001.

[2] Chumak, A. V.; Vasyuchka, V. I. and Hillebrands, B., Magnon spintronics. *Nat. Phys.* **2015**, 11, 453461.

[3] Urazhdin, S.; Demidov, V. E.; Ulrichs, H.; Kendziorczyk, T.; Kuhn, T.; Leuthold, H.; Wilde, G. and Demokritov, S. O., Nanomagnonic devices based on the spin-transfer torque. *Nat. Nanotech.* **2014**, 9, 509513.

[4] Vogt, K.; Fradin, F. Y.; Pearson, J. E.; Bader, S. D.; Hillebrands, B.; Hoffmann, A.; and Schultheiss, H., Realization of a spin-wave multiplexer. *Nat. Commun.* **2014**, 5, 3727.

[5] Sato, N.; Sekiguchi, K. and Nozaki, Y., Electrical demonstration of spin-wave logic operation. *Appl. Phys. Expr.* **2013**, 6, 063001.

[6] Kruglyak, V.V.; Demokritov, S.O., and Grundler, D., Magnonics. *J. Phys. D: Appl. Phys.* **2010**, 43, 264001.

[7] Khitun, A.; Bao, M. and Wang, K. L., Magnonic logic circuits. *J. Phys. D: Appl. Phys.* **2010**, 43, 264005.

[8] Denning, P. J. and Lewis, T. G., Exponential laws of computing growth. *Commun. ACM* **2016**, 60, 54-65.

[9] Zingsem, B. W.; Feggeler, T.; Terwey, A.; Ghaisari, S.; Spoddig, D.; Faivre, D.; Meckenstock, R.; Farle, M.; Winklhofer, M., Biologically encoded magnonics. *Nat. Commun.* **2019**, 85, 4345.

[10] Frömter, R.; Kloodt, F.; Röler, S.; Frauen, A.; Staeck, P.; Cavicchia, D. R.; Bocklage, L.; Röbisch, V.; Quandt, E. and Oepen, H. P., Time-resolved scanning electron microscopy with polarization analysis. *Appl. Phys. Lett.* **2016**, 108, 142401.

[11] Krasyuk, A.; Oelsner, A.; Nepijko, S. A.; Kuksov, A.; Schneider, C. M. and Schönhense, G., Time-resolved photoemission electron microscopy of magnetic field and magnetization changes. *Appl. Phys. A-Mater.* **2003**, 76, 863-868.

[12] Vogel, J.; Kuch, W.; Bonfim, M.; Camarero, J.; Pennec, Y.; Offi, F.; Fukumoto, K.; Kirschner, J.; Fontaine, A. and Pizzini, S., Time-resolved magnetic domain imaging by x-ray photoemission electron microscopy. *Appl. Phys. Lett.* **2003**, 82, 2299.

[13] Park, H. S.; Spencer Baskin, J.; Zewail, A. H., 4D Lorentz Electron Microscopy Imaging: Magnetic Domain Wall Nucleation, Reversal, and Wave Velocity. *Nano Lett.* **2010**, 10, 3796-3803.

[14] Schliep, K. B.; Quarterman, P.; Wang, J.-P. and Flannigan, D. J., Picosecond Fresnel transmission electron microscopy. *Appl. Phys. Lett.* **2017**, 110, 222404.

[15] Rubiano da Silva, N.; Möller, M.; Feist, A.; Ulrichs, H.; Ropers, C.; and Schäfer, S., Nanoscale Mapping of Ultrafast Magnetization Dynamics with Femtosecond Lorentz Microscopy. *Phys. Rev. X* **2018**, 8, 031052.

[16] Bonetti, S.; Kukreja, R.; Chen, Z.; Spoddig, D.; Ollefs, K.; Schöppner, Ch.; Meckenstock, R.; Ney, A.; Pinto, J.; Houanche, Frisch, J.; Stöhr, J.; Dürr, H. A.; Ohldag, H., Microwave soft x-ray microscopy for nanoscale magnetization dynamics in the 510 GHz frequency range. *Rev. Sci. Instr.* **2015**, 86, 093703.

[17] Schaffers, T.; Meckenstock, R.; Spoddig, D.; Feggeler, T.; Ollefs, K.; Schöppner, Ch.; Bonetti, S.; Ohldag, H.; Farle, M.; and Ney, A., The combination of microresonators with spatially resolved ferromagnetic resonance. *Rev. Sci. Instrum.* **2017**, 88, 093703.

[18] Goulon, J.; Rogalev, A.; Wilhelm, F.; Jaouen, N.; Goulon-Ginet, C.; Brouder, C., X-ray detected ferromagnetic resonance in thin films. *Eur. Phys. J. B* **2006**, 53, 169-184.

[19] Dürr, H. A.; Eimüller, T.; Elmers, H.-J.; Eisebitt, S.; Farle, M.; Kuch, W.; Matthes, F.; Mertins, M.; Mertins, H.-C.; Oppeneer, P. M.; Plucinski, L.; Schneider, C. M.; Wende H.; Wurth, W.; Zabel H., A Closer Look Into Magnetism: Opportunities With Synchrotron Radiation. *IEEE Trans. Magn.* **2009**, 45, 15.

[20] Van der Laan, G.; Figueroa, A. I., X-ray magnetic circular dichroismA versatile tool to study magnetism. *Coordin. Chem. Rev.* **2014**, 95, 277-278.

[21] Narkowicz, R.; Suter, D.; and Stonies, R., Planar microresonators for EPR experiments. *J. Magn. Reson.* **2005**, 175, 275-284.

[22] DSMZ,*Magnetospirillum magnetotacticum DSM 3856* **2019**.

[23] Zhu, X.; Hitchcock, A. P.; Bazylinski, D. A.; Denes, P.; Joseph, J.; Lins, U.; Marchesini, S.; Shiu, H. W.; Tyliszczak, T.; and Shapiro, D. A., Measuring spectroscopy and magnetism of extracted and intracellular magnetosomes using soft X-ray ptychography. *Proc. Natl. Acad. Sci. U. S. A.* **2016**, 113, E8219-E8227.

[24] Posfai, M.; Lefvre, C. T.; Trubitsyn, D.; Bazylinski, D. A.; and Frankel, R. B., Phylogenetic significance of composition and crystal morphology of magnetosome minerals. *Front. Microbiol.* **2013**, 4, 1-15.

[25] Frankel, R. B.; Blakemore, R. and Wolfe, R. S., Magnetite in Freshwater Magnetotactic Bacteria. *Science* **1979**, 203, 1355-1356.

[26] Maratea, D. and Blakemore, R., Aquaspirillum magnetotacticum sp. nov., a Magnetic Spirillum. *Int. J. Syst. Bacteriol.* **1981**, 31, 452-455.

[27] Faivre, D. and Schüler, D., Magnetotactic Bacteria and Magnetosomes. Chem. Rev. **2008**, 108, 4875-4898.

[28] Schleifer, K. H.; Schüler, D.; Spring, S.; Weizenegger, M.; Amann, R.; Ludwig, W.; and Köhler, M., The genus Magnetospirillum gen. nov., description of Magnetospirillum gryphiswaldense sp. nov. and transfer of Aquaspirillum magnetotacticum to Magnetospirillum magnetotacticum comb. nov. *Syst. Appl. Microbiol.* **1991**, 14, 379-385.

[29] Thompson, A. C.; Kirz, J.; Attwood, D. T.; Gullikson, E. M.; Howells, M. R.; Kortright, J. B.; Liu, Y.; Robinson, A. L.; Underwood, J. H.; Kim, K.-J.; Lindau, I.; Pianetta, P.; Winick, H.; Williams, G. P.; Scofield, J. H., *X-Ray Data Booklet*. 3rd ed., Lawrence Berkeley National Laboratory University of California: Berkeley CA, **2009**.

[30] Fairchild, M.D., *Color Appearance Models*. 3rd ed., John Wiley & Sons: Chichester, 2013.

[31] Vansteenkiste, A.; Leliaert, J.; Dvornik, M.; Helsen, M.; Garcia-Sanchez, F. and Van Waeyenberge, B., The design and verification of MuMax3. *AIP Adv.* **2014**, 4, 107133.

[32] Exl, L.; Bance, S.; Reichel, F.; Schrefl, T.; Stimming, H. P.; and Mauser, N. J., LaBonte's method revisited: An effective steepest descent method for micromagnetic energy minimization. *J. Appl. Phys.* **2014**, 115, 17D118.

[33] Aragón, R., Buttrey, D. J., Shepherd, J. P., Honig, J. M., Influence of nonstoichiometry on the Verwey transition, *Phys. Rev. B* **1985**, 31, 430-436.

[34] Kąkol, Z., Honig, J. M., Influence of deviations from ideal stoichiometry on the anisotropy parameters of magnetite $Fe_{3(1-\delta)}O_4$, *Phys. Rev. B* **1989**, 40, 9090-9097.

[35] Wu, H.-C., Arora, S. K., Mryasov, O. N., Shvets, I. V., Antiferromagnetic interlayer exchange coupling between Fe_3O_4 layers across a nonmagnetic MgO dielectric layer, *Appl. Phys. Lett.* **2008**, 92, 182502.

[36] Charilaou, M.; Winklhofer, M. and Gehring, A. U., Simulation of ferromagnetic resonance spectra of linear chains of magnetite nanocrystals. *J. Appl. Phys.* **2011**, 109, 093903.

[37] Zingsem, B.; Feggeler, T.; Meckenstock, R.; Schaffers, T.; Pile, S.; Ohldag, H.; Farle, M.; Wende, H.; Ney, A.; Ollefs, K., *arXiv:1901.10595 [cond-mat.str-el]*, **2019**.

[38] Schaffers, T.; Feggeler, T.; Pile, S.; Meckenstock, R.; Buchner, M.; Spoddig, D.; Ney, V.; Farle, M.; Wende, H.; Wintz, S.; Weigand, M.; Ohldag, H.; Ollefs, K.; Ney, A., Evaluation protocol for revealing magnonic contrast in STXM-FMR measurements. *Nanomaterials (Basel)* **2019**, 9, 1-13.

[39] Chumak, A. V.; Serga, A. a. and Hillebrands, B., Magnon transistor for all-magnon data processing. *Nat. Commun.* **2014**, 5, 4700.

[40] Barman, A.; Gubbiotti, G.; Ladak, S.; Adeyeye. A. O.; Krawczyk, M.; Gräfe, J.; Adelmann, C.; Cofofana, S.; Naeemi, A.; Vasyuchka, V. I.; Hillebrands, B.; Nikitov, S. A.; Yu, H.; Grundler, D.; Sadovnikov, A.; Grachev, A. A.; Sheshukova, S. E.; Duquesne, J.-Y.; Marangolo, M.; Gyorgy, C.; Porod, W.; Demidov, V. E.; Urazhdin, S.; Demokritov, S.; Albisetti, E.; Petti, D.; Bertacco, R.; Schultheiss, H.; Kruglyak, V. V.; Poimanov, V. D.; Sahoo, A. K.; Sinha, J.; Yang, H.; Muenzenberg, M.; Moriyama, T.; Mizukami, S.; Landeros, P.; Gallardo, R. A.; Carlotti, G.; Kim, J.-V.; Stamps, R. L.; Camley, R. E.; Bivas, R.; Otani, Y; Yu, W.; Yu, T.; Bauer, G. E. W.; Back, C. H.; Goetz, S. U.; Dobrovolskiy, O. V.; van Dijken, S.; Budinska, B.; Qin, H.; Chumak, A.; Khitun, A.; Nikonov, D. E.; Young, I. A.; Zingsem, B. and Winklhofer, M., The 2021 Magnonics Roadmap. *J. Phys.: Condens. Matter* **2021**, in press, DOI: 10.1088/1361-648X/abec1a.

[41] Chao, W., Fischer, P.; Tyliszczak, T.; Rekawa, S.; Anderson, E.; and Naulleau, P., Real space soft x-ray imaging at 10 nm spatial resolution. *Opt. Express* **2012**, 20, 9777-9783.

Supplemental

Spatially resolved GHz magnetization dynamics of a magnetite nano-particle chain inside a magnetotactic bacterium

T. Feggeler,[1*] R. Meckenstock,[1] D. Spoddig,[1] B. Zingsem,[1,2] H. Ohldag,[3,4**]
H. Wende,[1] M. Farle,[1,5] M. Winklhofer,[5] and K. Ollefs[1]

[1]Faculty of Physics and Center for Nanointegration Duisburg-Essen (CENIDE), University of Duisburg-Essen, 47048 Duisburg, Germany
[*] Present address: Advanced Light Source, Lawrence Berkeley National Laboratory, Berkeley, CA, United States
[2]Ernst Ruska Centre for Microscopy and Spectroscopy with Electrons and Peter Grünberg Institute, Forschungszentrum Jülich GmbH, 52425 Jülich, Germany
[3]SLAC National Accelerator Laboratory, 94025 Menlo Park, CA, United States
[4]Department of Physics, University of California Santa Cruz, Santa Cruz CA 95064, United States
[**]Present address: Advanced Light Source, Lawrence Berkeley National Laboratory, Berkeley, CA, United States and Department of Material Sciences and Engineering, Stanford University, Stanford CA 94305, United States
[5]Kirensky Institute of Physics, Federal Research Center KSC SB RAS, Russia
[6]School of Mathematics and Science, University of Oldenburg, 26129 Oldenburg, Germany

I. Time resolved setup

X-ray microscopy was performed using the Scanning Transmission X-ray Microscopy (STXM) setup at beamline 13.1 at the Stanford Synchrotron Radiation Lightsource (SSRL) at SLAC National Accelerator Laboratory. Monochromatic soft X-rays with tunable polarization produced by an elliptical undulator are focused on the sample with a Fresnel zone plate to a spot size of ∼ 50 nm. The thin sample can be scanned in two dimensions, while the transmitted X-rays are detected using a photodiode, thus producing a 2D image of the transmission of the sample for the chosen combination of photon energy and polarization. To achieve time resolution a dedicated setup was used as described in detail in [1]. The principle of the setup shown in figure S1 is described for convenience in the following here as well. A synchrotron is a pulsed source of x-rays and at the SSRL the pulse frequency is ~476 MHz corresponding to a pulse interval of 2.1 ns. A maximum of 372 individual x-ray pulses can so be realized with every turn. However, not all pulses are equally intense. There are intensity variations of the order of 10% between pulses and one particular pulse – the camshaft – is 5 times as bright and serves as a marker bunch to indicate a full turn of the synchrotron. At SSRL the frequency with which the camshaft – or every other bunch for that matter - reappears is 1.28 MHz or every 781 ns. X-ray pulses transmitted through the sample will be registered with an avalanche photodiode, operated in reverse bias mode. The thickness of the sample as well as incoming intensity is such that only for a few (~10 %) X-ray bunches a single X-ray photon will be transmitted through the sample. We have confirmed with an oscilloscope that multiphoton events are rare (~1 %), so that counting X-ray pulses is equivalent to measuring transmitted X-ray intensity. The pulses are recorded by a setup based on a Field Programmable Gate Array (FPGA) and can be routed to one of 16 individual counters in a software defined matter [2] based on its number (1 to 372) in the ring or if it came from an odd or even turn of the synchrotron. One counter can be assigned to a user defined number of pulses in that way.

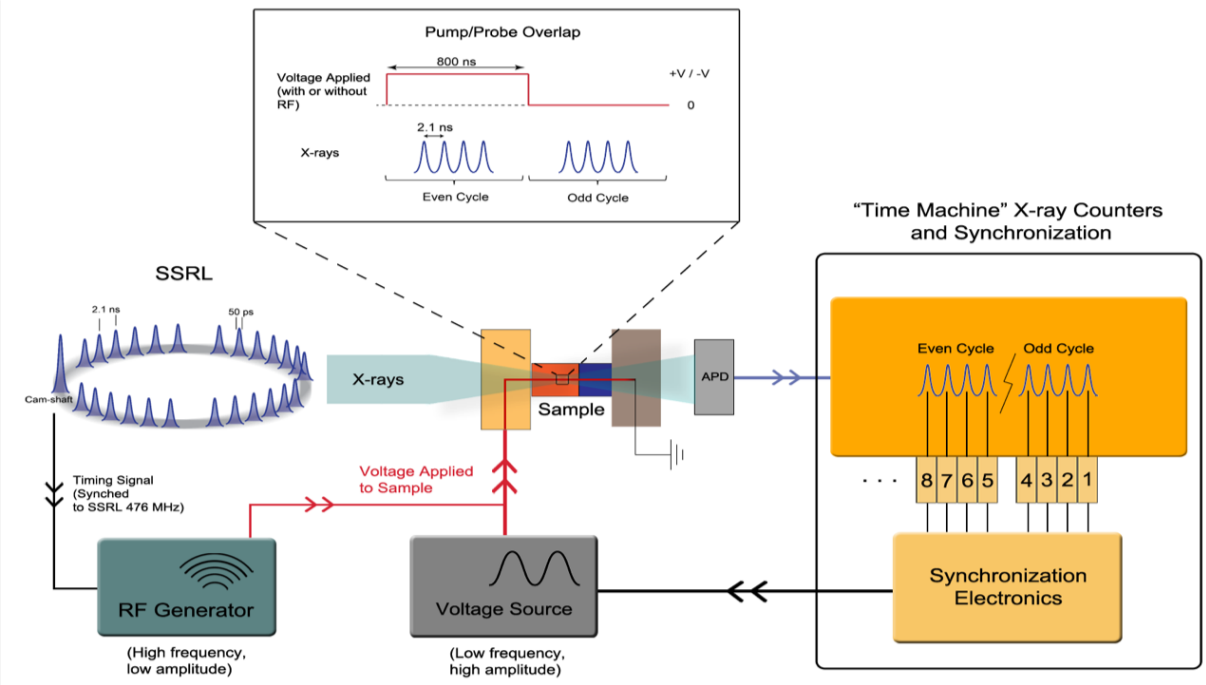

Figure S1: Schematic representation of the time resolved measurement technique.

For time resolved measurements an external excitation also has to be synchronized with the X-ray probe. For the microwave experiments this is achieved by using a phase locked loop that compares the output of a microwave generator with the n^{th} harmonic of the synchrotron driving frequency f and adjusts the output frequency of the generator accordingly Using this approach a relative stability in the phase of 1 ps over 24 hours was achieved [1]. In fact the generator is not synchronized with just n*f but with (n+1/6)*f, so that the relative phase of the RF advances by 60 degree between subsequent synchrotron pulses. By routing the signal of subsequent pulses to different counters in the appropriate order we can now measure the response of the X-ray transmission of the sample to the external microwave at the start phase as well as 60, 120, 180, 240 and 300 degree later. The expected change in X-ray transmission as response to the RF excitation is small, less than 0.1% in many cases, which requires a way to normalize the detected signal. For this purpose, we can turn off the excitation for every second turn of the synchrotron and measure the ground state of the sample. This corresponds effectively to a double lock-in approach using the two intrinsic frequencies of the synchrotron (the bunch frequency of 476 MHz and the camshaft frequency of 1.28 MHz) as reference. A sensitivity to magnetic signals of 0.001% has been demonstrated in this way [3].

II. Discussion of the origin of the oscillating background

The phase and amplitude analysis presented in Figure 3b) reveals a visible oscillating background around the location of the Fe_3O_4 nanoparticle chain, showing an inhomogeneously distributed relative phase with a phase differing between about 270° to 300°. There are multiple possible physical origins of the oscillating background all attributed to various crosstalk effects affecting the counts on the avalanche photo diode, which do not originate from a ferromagnetic resonance signal. In [4] the influence of standing waves generated by the microwave within the antenna like cabeling of the avalanche photodiode resulting in additional counts is stated. Furthermore, an interaction between charge carriers generated by the incident X-rays at the underlying C-TEM grid and the microwave takes place, which is also the case for the biomass surrounding the sample Fe_3O_4 nano particle chain. A negligible impact is expected from heating effects due to the power of the incident microwave radiation of about 800 mW. All microwave induced effects are also expected to take place in a reduced magnitude during the microwave off state, as the microwave power is only attenuated by 30 dB and therefore not turned off completely, still resulting in a remaining microwave power level of about 1 mW. The "time machine" component of the time resolved setup (Figure S1) acts as a discriminator on the signal input side. To avoid the loss of sample contributions to the signal the discriminator threshold is set to accept a wider signal range, resulting in additional noise. The general signal origin is X-ray absorption, which is described in terms of the Lambert-Beer law [5] incorporating

an exponential dependence of the X-ray absorption cross-section. To largely eliminate the background signal, we hence take the natural logarithm of the division of microwave on and off data and extract hereby the ferromagnetic resonance induced X-ray transmission. To further reduce the background contributions to the signal and thereby enhance the visibility of the resonant response of the chain measured by STXM- FMR, an offset of 250000 counts to the data is subtracted before further data analysis.

III. References

1. S. Bonetti, R. Kukreja, Z. Chen, D. Spoddig, K. Ollefs, C. Schöppner, R. Meckenstock, A. Ney, J. Pinto, R. Houanche, J. Frisch, J. Stöhr, H.A. Dürr, and H. Ohldag, *Microwave soft x-ray microscopy for nanoscale magnetization dynamics in the 5–10 GHz frequency range.* Review of Scientific Instruments, 2015. **86**(9): p. 093703-1-093703-9.
2. Y. Acremann, V. Chembrolu, J.P. Strachan, T. Tyliszczak, and J. Stöhr, *Software defined photon counting system for time resolved x-ray experiments.* Review of Scientific Instruments, 2007. **78**(1): p. 014702-1-014702-4.
3. R. Kukreja, S. Bonetti, Z. Chen, D. Backes, Y. Acremann, J.A. Katine, A.D. Kent, H.A. Dürr, H. Ohldag, and J. Stohr, *X-ray Detection of Transient Magnetic Moments Induced by a Spin Current in Cu.* Physical Review Letters, 2015. **115**(9): p. 096601-1-096601-5.
4. T. Schaffers, T. Feggeler, S. Pile, R. Meckenstock, M. Buchner, D. Spoddig, V. Ney, M. Farle, H. Wende, S. Wintz, M. Weigand, H. Ohldag, K. Ollefs, and A. Ney, *Extracting the Dynamic Magnetic Contrast in Time-Resolved X-ray Transmission Microscopy.* Nanomaterials (Basel), 2019. **9**(7): p. 1-13.
5. J. Stöhr and H.C. Siegmann, *Magnetism From Fundamentals to Nanoscale Dynamics*. Springer Series in solid-state sciences, ed. M. Cardona, et al. 2006, Berlin, Heidelberg: Springer.